High-energy-density plasma in femtosecond-laser-irradiated nanowire-array targets for nuclear reactions

View Online   Export Citation   CrossMark

Defeng Kong,[1] (iD) Guoqiang Zhang,[2,a)] Yinren Shou,[1] (iD) Shirui Xu,[1] Zhusong Mei,[1] (iD) Zhengxuan Cao,[1] (iD)
Zhuo Pan,[1] Pengjie Wang,[1] (iD) Guijun Qi,[1] Yao Lou,[2] Zhiguo Ma,[3] Haoyang Lan,[1,4] Wenzhao Wang,[5] (iD)
Yunhui Li,[6] (iD) Peter Rubovic,[7,8] (iD) Martin Veselsky,[7] Aldo Bonasera,[9,10] Jiarui Zhao,[1] Yixing Geng,[1]
Yanying Zhao,[1] Changbo Fu,[3] Wen Luo,[4] (iD) Yugang Ma,[2,3] Xueqing Yan,[1,11,12] (iD) and Wenjun Ma[1,11,12,a)] (iD)

AFFILIATIONS

[1] State Key Laboratory of Nuclear Physics and Technology, and Key Laboratory of HEDP of the Ministry of Education, CAPT, School of Physics, Peking University, Beijing 100871, China
[2] Shanghai Institute of Applied Physics, Chinese Academy of Sciences, Shanghai 201800, China
[3] Key Laboratory of Nuclear Physics and Ion-Beam Application (MOE), Institute of Modern Physics, Fudan University, Shanghai 200433, China
[4] School of Nuclear Science and Technology, University of South China, Hengyang 421001, China
[5] INPAC and School of Physics and Astronomy, Shanghai Jiao Tong University, Shanghai 200240, China
[6] Shenzhen Institutes of Advanced Technology, Chinese Academy of Sciences, Shenzhen 518055, China
[7] Institute of Experimental and Applied Physics, Czech Technical University in Prague, Husova 240/5, 11000 Prague 1, Czech Republic
[8] ELI Beamlines Center, Institute of Physics of the Czech Academy of Sciences, 252 41 Dolní Břežany, Czechia
[9] Cyclotron Institute, Texas A&M University, College Station, Texas 77843, USA
[10] Laboratori Nazionali del Sud, INFN, via Santa Sofia, 62, Catania 95123, Italy
[11] Beijing Laser Acceleration Innovation Center, Huairou, Beijing 101400, China
[12] Collaborative Innovation Center of Extreme Optics, Shanxi University, Taiyuan, Shanxi 030006, China

[a)] Authors to whom correspondence should be addressed: zhangguoqiang@zjlab.org.cn and wenjun.ma@pku.edu.cn

ABSTRACT

In this work, the high-energy-density plasmas (HEDP) evolved from joule-class-femtosecond-laser-irradiated nanowire-array (NWA) targets were numerically and experimentally studied. The results of particle-in-cell simulations indicate that ions accelerated in the sheath field around the surfaces of the nanowires are eventually confined in a plasma, contributing most to the high energy densities. The protons emitted from the front surfaces of the NWA targets provide rich information about the interactions that occur. We give the electron and ion energy densities for broad target parameter ranges. The ion energy densities from NWA targets were found to be an order of magnitude higher than those from planar targets, and the volume of the HEDP was several-fold greater. At optimal target parameters, 8% of the laser energy can be converted to confined protons, and this results in ion energy densities at the GJ/cm^3 level. In the experiments, the measured energy of the emitted protons reached 4 MeV, and the changes in energy with the NWA's parameters were found to fit the simulation results well. Experimental measurements of neutrons from $^2H(d,n)^3He$ fusion with a yield of $(24 \pm 18) \times 10^6/J$ from deuterated polyethylene NWA targets also confirmed these results.

I. INTRODUCTION

Far away from the Earth, high-energy-density plasma (HEDP) exists in many areas of the universe, for example, in the cores of planets and stars.[1] Understanding and controlling this form of matter would help us to unveil the origins of heavy elements[2] and harness future nuclear-energy technologies.[3] Thanks to the development of high-power lasers, we can now create HEDP in the lab by compressing and heating a spherical capsule using multiple-megajoule nanosecond lasers. This state of matter has been the subject of worldwide research focus, and it is expected to help achieve self-sustainable reactions in inertial confinement fusion (ICF).[4–7] In addition, research around HEDP has also promoted the development of laser nuclear physics,[8–15] laboratory astrophysics,[16,17] and high-energy-density physics.[18–20]

Apart from the well-known ICF scheme, HEDP can be created using ultra-intense and ultrashort laser pulses by virtue of relativistic laser–plasma interactions. An ultra-intense laser field can deeply ionize a target and accelerate its electrons to MeV levels on femtosecond timescales,[21] forming a strong micron-scale space-charge field that can drive its ions. The most common experimental scheme for this involves irradiating a solid foil target at ultra-high intensity. The laser pulse interacts with the front surface of the foil, generating supra-thermal electrons in an expanded dilute plasma. Heated by these supra-thermal electrons and the return current, the solid target becomes an HEDP. The drawback of this scheme is that if we are interested in nuclear reactions in the HEDP, the entirety of the solid foil will not be hot enough for these to occur. The indirect heating involved results in a considerable temperature gradient in the foil,[22] and only a small number of ions close to the surface will reach a temperature sufficient for nuclear reactions. To overcome this problem, cluster targets produced from cryogenic high-density gas[12–14] or low-density foam[23–26] have been used. The laser pulse can propagate through these materials and volumetrically heat the nanometer-sized clusters or the foam's building blocks, resulting in the production of an HEDP. However, the densities of these plasmas typically do not exceed 1% of the solid density, which is unfavorable for nuclear reactions.

Recently, an increasing amount of attention has been paid to the use of novel microstructured targets to acquire near-solid-density HEDPs.[27–33] In this area of research, nanowire-array (NWA) targets have shown superior performance. Numerical and experimental studies have indicated that NWA targets can absorb the majority of the laser energy and significantly enhance the energy-conversion efficiency to plasma when compared to solid targets,[34–36] producing homogeneous HEDP with near-solid density. Figure 1(a) shows a schematic diagram of an NWA target. The typical diameter (D), length (L), and spacing (S) of the nanowires (NWs) are tens to hundreds of nanometers, 1–10, and 0.1–1.0 μm, respectively. The heating process of an NWA target under ultra-intense laser irradiation is illustrated in Fig. 1(b).

An NWA's structure allows a laser pulse to propagate inside the target and interact with the sidewalls of the NWs. Electrons in the skin depth of NWs are pulled out into gaps and can be accelerated to tens of MeV in the laser field. On top of their quiver motions, these electrons collectively move along the laser propagation direction due to the $\mathbf{v} \times \mathbf{B}$ force. The resulting return current (typically of the order of 10^1–10^2 kA)[37,38] inside the NWs and the reciprocal bombardment of the supra-thermal electrons accelerated by $\mathbf{J} \times \mathbf{B}$ heating[39] efficiently heat the NWs to a high temperature. It has been found that the electron temperatures can reach values of 0.1[38] and 0.9 MeV[39] under the effects of the return current and $\mathbf{J} \times \mathbf{B}$ heating with laser amplitudes of $a = 2$ and 5, respectively. Furthermore, the escaped electrons also give rise to a space-charge field (sheath field) normal to the surfaces of the NWs. Ions can subsequently be accelerated to MeV-level energies in this sheath field,[40,41] which also contributes to plasma heating, with temperatures reaching the MeV level when they are stopped by nearby NWs. More details of these interactions, such as the plasma compression due to Z-pinch formation under higher-intensity petawatt (PW) lasers,[38] are still under exploration. The electron temperatures can reach 4 MeV at a laser amplitude of $a = 17$.

The emissions of energetic electrons,[37,42] ions,[43,44] x-/γ-rays,[45–48] and neutrons[49,50] from NWA plasmas have been extensively observed. Purvis et al. measured the x-rays from Ni and Au NWA targets irradiated with 0.5 J femtosecond laser pulses.[45] They observed the production of 100-fold-enhanced line emission over planar solid targets. Using numerical simulations, they concluded that the electron energy density (EED) after the expansion of the NWs is 0.3 GJ/cm³, which is comparable to that of spherical compression at the National Ignition Facility with megajoule laser
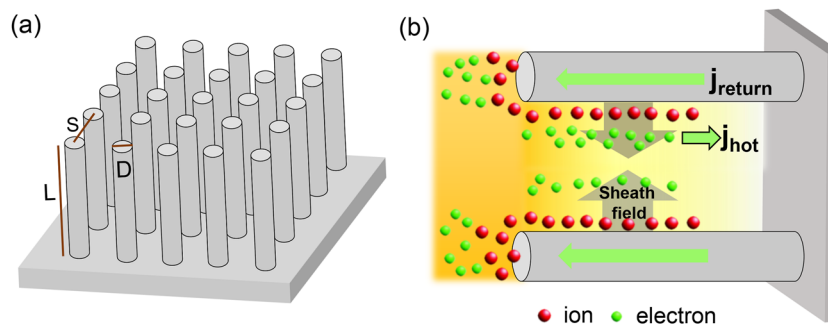
FIG. 1. (a) Schematic diagram of an NWA target; L, D, and S are the NW length, diameter, and spacing, respectively. (b) Schematic showing plasma heating and ion acceleration in an NWA target.

pulses.[51] Later, they increased the laser energy to 10 J[52] and observed intense line emission from Au^{72+} ions due to the >100 GJ/cm^3 EED. Naturally, such a high energy density attracts interest regarding thermonuclear reactions. Deuterium–deuterium fusion in an NWA was first reported in 2018 by using deuterated polyethylene NWA targets.[47] This produced a neutron yield of 10^6/J/shot, a record for a joule-scale laser. Recently, 10^7/shot neutrons were measured at a higher intensity with a PW laser.[50]

The electron-heating dynamics and EED in NWA targets have been widely studied by measuring the core–shell x-ray emissions from high-Z NWAs. Regrettably, this method is not applicable to low-Z NWA targets, which are particularly important for fusion-energy-oriented reactions such as ^{2}H(d,n)^{3}He and ^{11}B(p,2α)α. Furthermore, the energy density of ions in NWA targets, which is of foremost importance for nuclear reactions, has rarely been discussed. Finding the optimal target parameters for fusion nuclear reactions and additional methods for characterizing the high-energy-state in addition to x-ray spectroscopy will require further study.

In this work, first, we examined the interactions between NWA targets and femtosecond laser pulses by employing collisional 2D particle-in-cell (PIC) simulations. The electron and ion (proton) energy densities of the NWA targets across a broad target parameter range were obtained and compared to those of planar targets. The confined and emitted protons were defined, and their interrelationship and contributions to the energy densities of the HEDP were thoroughly examined. Thereafter, we experimentally measured the emitted protons, deuterium ions, and neutrons from ^{2}H(d,n)^{3}He fusion using ordinary and deuterated polyethylene NWA targets. The results were found to confirm those of our simulations.

## II. LASER–NWA INTERACTION, CONFINED AND EMITTED PROTONS

To illustrate the interaction of NWA targets with relativistic femtosecond pulses, 2D PIC simulations were performed using the current EPOCH[53] code. In the model for these simulations, the simulation box had a size of $40\lambda_L \times 50\lambda_L$ with 4000×5000 cells in the $x \times y$ dimensions (laser wavelength $\lambda_L = 0.8$ μm). The box boundary in the y direction was periodic. A laser pulse polarized linearly in the y direction with a Gaussian profile of $a_y = a_0 e^{-(r/\sigma_0)^2} e^{-(t-t_0)^2/\tau^2}$ traveled along the x axis from the left side and was normally incident on the NWA target, where $a_0 = eE_0/m_e c\omega_L = 5$, $\sigma_0 = 4.3$ μm, and $\tau = 10\lambda_L/c = 26.7$ fs. The NWA's L, D, and S values were set according to the achievable target parameters in the experiments. The NWs were located in the region $0 < x < L$. The atomic ratio of C and H was 1:2, as in polyethylene. A 10 μm-thick polyethylene substrate was placed in the region $L < x < L + 10$ μm. The initial densities of electrons, protons, and C^{2+} ions were $80n_c$, $40n_c$, and $20n_c$, respectively. Here, $n_c = m_e\omega_L^2/4\pi e^2$ = 1.7×10^{21} cm^{-3} is the critical electron density, in which ω_L, e, and m_e are the laser frequency, electron charge, and electron mass, respectively. The entire target was cold (10 eV) and not fully ionized, and the optical field ionization was included in the setup. The numbers of macroparticles per cell of each ion species and electrons were 12 and 48, respectively.

Figure 2 shows the simulation results for a typical NWA target with D = 200 nm, S = 450 nm, and L = 5 μm. At a simulation time of t = 150 fs, the value of E_y in the gaps between the NWs oscillates along the x direction with a spatial period of λ_L. This indicates that the driving laser can propagate as deep as 5 μm below the surface. In contrast, the laser–plasma interaction for a planar target is limited to the skin depth at the surface, and most of the laser energy is reflected. Figure 2(b) compares the absorbed laser energy and the fraction of the laser energy converted into ions and electrons for an NWA target and a planar target. The total absorption ratio of 70% for the NWA is five times that of the planar targets. Unlike planar targets, in which the electrons absorb almost all the energy, in NWA targets, about 18% and 50% of the laser energy is converted into ions and electrons, respectively. Driven by the penetrating laser field, electrons from the surfaces of the NWs are drawn into the gaps and accelerated. The electron density at t = 210 fs is shown in Fig. 2(c). As a result of the charge separation, a sheath field is built around the NWs.[54] The spatial distribution of the electric field E_{sy} is depicted in Fig. 2(d). A line of E_{sy} is plotted along the y axis at x = 4 μm. The oscillating E_{sy}, which points outward from the NWs, has a maximum strength of 3×10^{12} V/m. Ions from the NWs can gain energy in E_{sy} and be laterally accelerated into the gaps. For simplicity of discussion, we choose protons as the representative ions and depict their distribution in Figs. 2(e) and 2(f). It can be seen that the NWA evolves into a homogeneous plasma with time. All the laterally accelerated protons are eventually stopped in the target, which, together with the bulk protons in the NWs, can be defined as "confined protons." Aside from the confined protons, the electrons that have escaped from the NWs in the x direction build the field of E_{sx} [at x = 0 μm in Fig. 2(c)], which can accelerate protons from the tips of the NWs to high energy. The protons leaving the target can be called "emitted protons," and they can be found in the region $x < 0$ in Fig. 2(f).

The x–p_x phase diagram of protons at t = 460 fs is shown in Fig. 3(a). This clearly describes the characteristics of the confined and emitted protons. The emitted protons distributed at $x < 0$ have high p_x up to $-100m_e c$ (2.7 MeV), while the confined protons in the range $0 < x < 5$ μm have much higher values. The x–p_y phase diagram (inset) indicates that the confined protons have $|p_x| < 40m_e c$. The two groups of protons can also be distinguished from the angular distribution in Fig. 3(b). The emitted protons peak at 0°, while the confined protons are near to -90° and 90°. The dashed line in Fig. 3(b) shows the integrated energy of protons as a function of distribution angle. This indicates that the confined protons contain far more energy than the emitted protons, providing most of the plasma's proton energy density (PED). According to the above classification, the energy spectra of the two groups of protons are given in Fig. 3(c). The fitting lines show that the temperatures of the confined and emitted protons are 50 and 300 keV, respectively.

III. ENERGY DENSITY OF THE NWA PLASMA

The EED and PED of a typical NWA target (with the same parameters as in Fig. 2) and a planar target at t = 460 fs are depicted in Fig. 4. One can see that the NWA's EED peaks at 0.3 GJ/cm^3, about
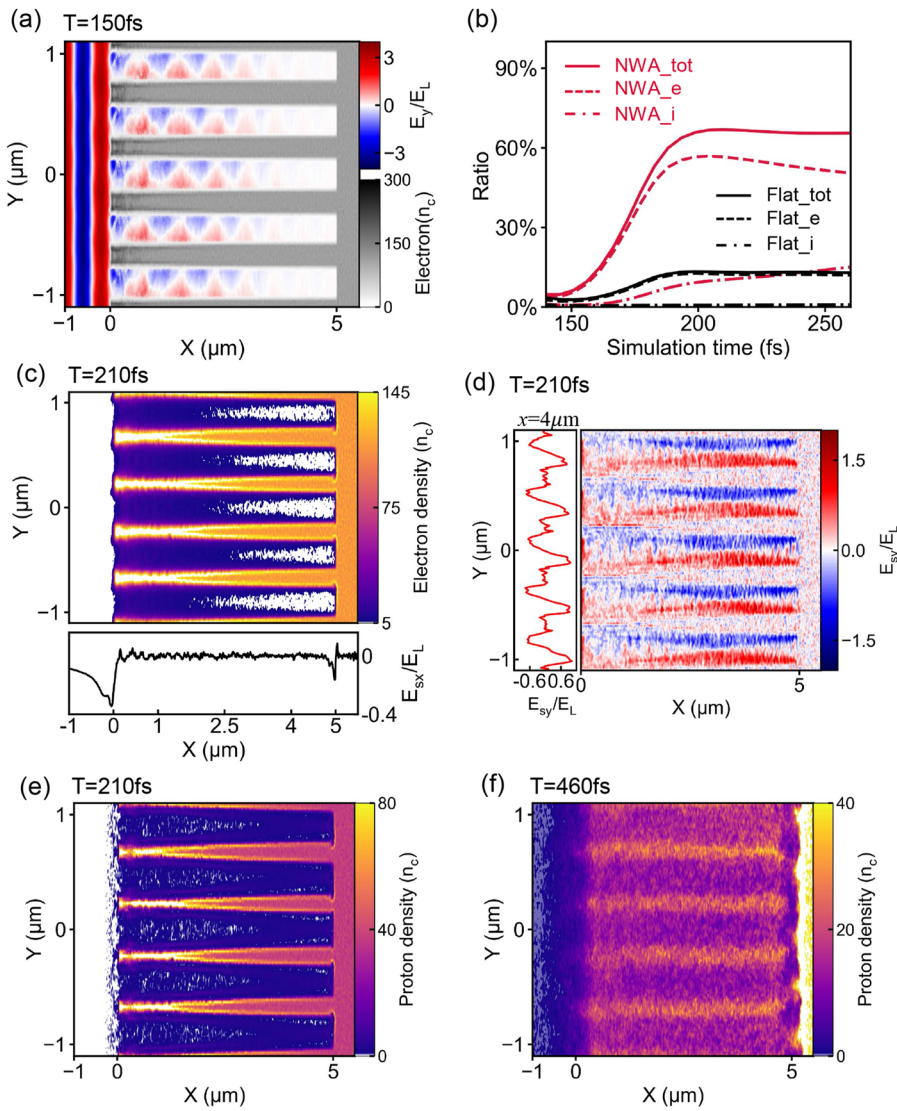
FIG. 2. 2D PIC simulation results. (a) Spatial distribution of the electric field E_y and electron density n_e at $t = 150$ fs. (b) Total laser absorption ratio and the fraction of the laser energy converted into ions and electrons over the simulation time for the planar and NWA targets. (c) Spatial distribution of the electron density at $t = 210$ fs; the black line shows the sheath field E_{sx} along the x axis at $y = 0$. (d) Spatial distribution of the sheath field E_{sy} at $t = 210$ fs; the red line shows the sheath fields E_{sy} along the y axis at $x = 4$ μm (e) and (f) Spatial distributions of the proton densities at $t = 210$ fs and $t = 460$ fs, respectively.
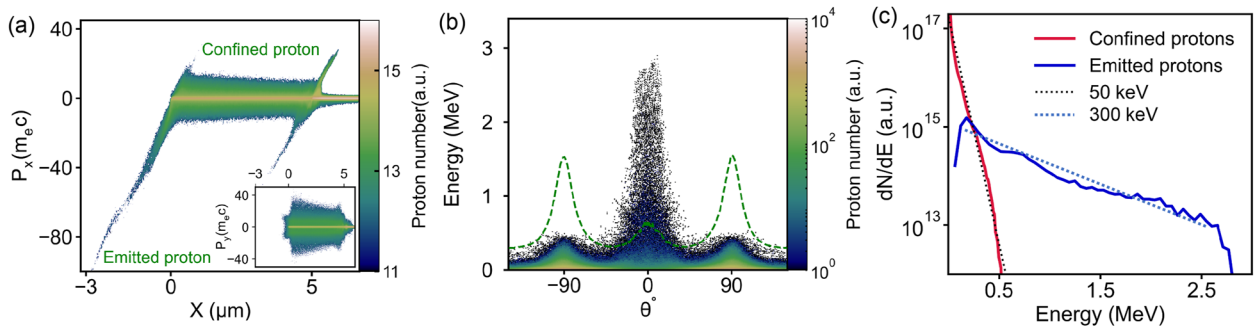
FIG. 3. Confined and emitted protons. (a) x–p_x and x–p_y phase diagrams of the protons at $t = 460$ fs. (b) Angular distribution of the protons at $t = 460$ fs; the green dashed line shows the integral of the energies at different angles. (c) Energy spectra of the confined and emitted protons at $t = 460$ fs; the dashed lines show the fitted temperatures of the protons.
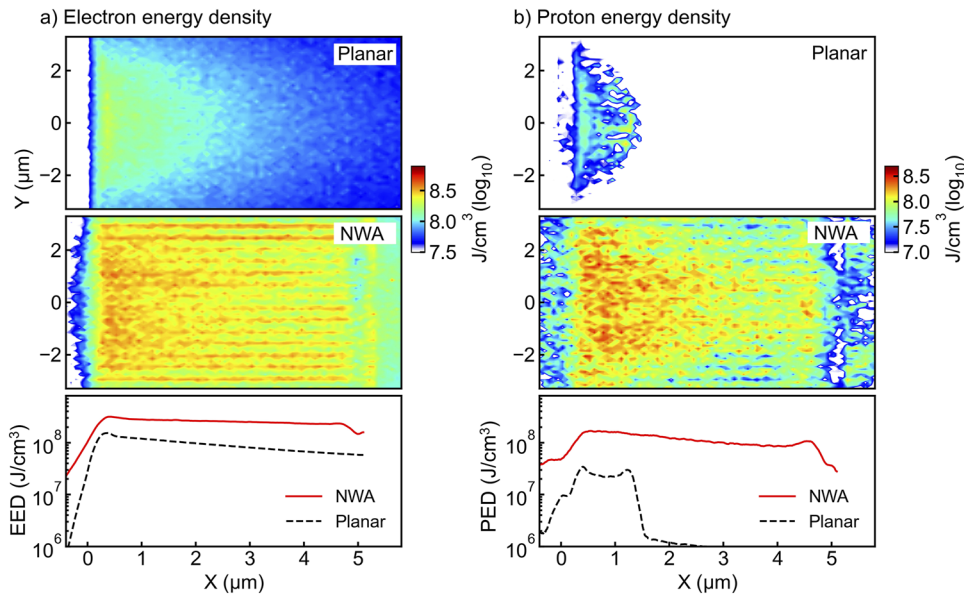
FIG. 4. Spatial distributions and line plots ($y = 0$) of (a) EED and (b) PED for a planar target and a typical NWA target at a simulation time of $t = 460$ fs.

three times that of the planar target. This enhancement is mainly due to the higher absorption of the laser energy. Since the energetic electrons can penetrate deeply into the bulk of the target, the volume of the high-energy-density region in the case of a planar target is not significantly smaller than in the case of an NWA target. Compared to the EED, the enhancement of the PED in the NWA target is much more prominent; the maximum PED is 0.2 GJ/cm^3, more than an order of magnitude greater than that of the planar target. Moreover,

it can be seen from Fig. 4(b) that the high-PED volume in the NWA is much larger than that of the planar target. In the planar target, the depth of the high-PED region is limited to 1 μm below the surface; in the NWA target, the high-PED region covers the whole target. This is because laterally accelerated protons are abundant in the NWA, and they carry a significant amount of energy.

To reveal the dependence of the PED on the target parameters of an NWA, we performed a series of simulations. Figures 5(a)–5(d)
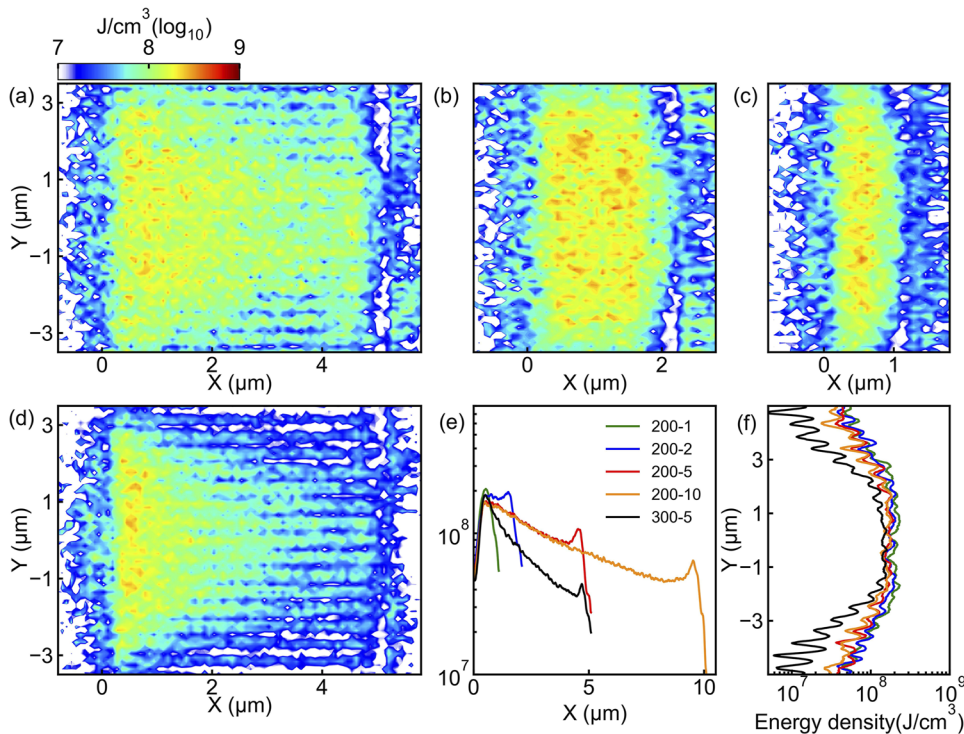
FIG. 5. Spatial distribution of PED for NWA targets with (a) $L = 5$ μm, (b) $L = 2$ μm, (c) $L = 1$ μm ($D = 200$ nm, $S = 450$ nm), and (d) $L = 5$ μm ($D = 300$ nm, $S = 450$ nm) (e) and (f) PEDs of different targets along the x and y directions, respectively.

show the spatial distributions of the PED of NWA targets with $L = 5$, 2, and 1 μm ($D = 200$ nm, $S = 450$ nm), and $L = 5$ μm ($D = 300$ nm, $S = 450$ nm), respectively. Figures 5(e) and 5(f) depict plots of the PED along the x and the y directions, respectively, and the data from an NWA of $L = 10$ μm, $D = 200$ nm, and $S = 450$ nm are also included. It can be seen that NWA targets with different lengths have almost the same maximum PED. Increasing the length of the NWs does not enhance the PED, but it does increase the volume of the high-PED region. In a given NWA, the PED decreases with x. For the $L = 10$ μm NWA, the PED drops to 0.05 GJ/cm^3 at $x = 10$ μm, which is about a quarter of the peak value at the surface. The decreasing gradient depends strongly on the value of D. The $D = 300$ nm NWA has a gradient that is double that of the $D = 200$ nm NWA. The total proton energy contained in the plasma is significantly lower as a result.

Figure 6 shows the laser absorption ratio, temperature of confined electrons, temperature and number of confined protons, and total energy of emitted and confined protons as functions of the NW's diameters and lengths. It should be noted that confined protons with energies lower than 1 keV are not counted in these data. As shown in Fig. 6(a), the laser absorption ratio is closely related to the NW diameter: smaller diameters correspond to higher absorption. This is because a larger diameter results in narrower gaps. The time before the complete filling of the gaps by overdense plasma is therefore, shorter, resulting in lower laser absorption and incomplete heating of the NWs. The temperatures of the confined electrons and protons and the numbers of >1 keV confined protons decrease with increasing diameter. It should be noted that the sheath field established by the electrons directly affects the acceleration and

heating of protons. Therefore, the electron temperature results in consistent changes in proton temperature with the NW parameters. However, a decreased diameter will reduce the average density of the target for a given value of S, which is unfavorable to higher proton numbers. Figure 6(b) shows that a moderate diameter of $D = 200$ nm is the best trade-off, for which the average density is 16% of the solid density, and energetic confined protons contain 63 mJ energy for 1 J of input laser energy.

With a fixed diameter of 200 nm, we varied the length of the NWs to study its influence on the NWA's PED. Figures 6(d) and 6(e) indicate that increasing the length of the NWs will not affect the laser absorption or the temperatures of the confined electrons and protons. This is understandable, as these parameters are determined by the laser–plasma interaction at the sidewalls of the NWs. In contrast, the number of confined protons is proportional to the length of the NWs. Moreover, as shown in Fig. 6(d), with increasing NW length, the energy converted to confined protons rises, while that converted to emitted protons drops. This is consistent with the observation in Fig. 5 that NWA targets with longer NWs have larger high-PED volumes. It can be seen that 9% of the laser energy is converted to protons in the best case ($L = 10$ μm), and the vast majority (>90%) of this is converted to confined protons.

In summary, our simulations explored the parameter space of NWAs for the purpose of establishing the values required for a high PED. It was established that the optimal NW diameter is 200 nm. With increasing NW length, the energy imparted to confined protons rises, whereas that imparted to emitted protons declines. NWA targets with an NW length of 10 μm and an NW diameter
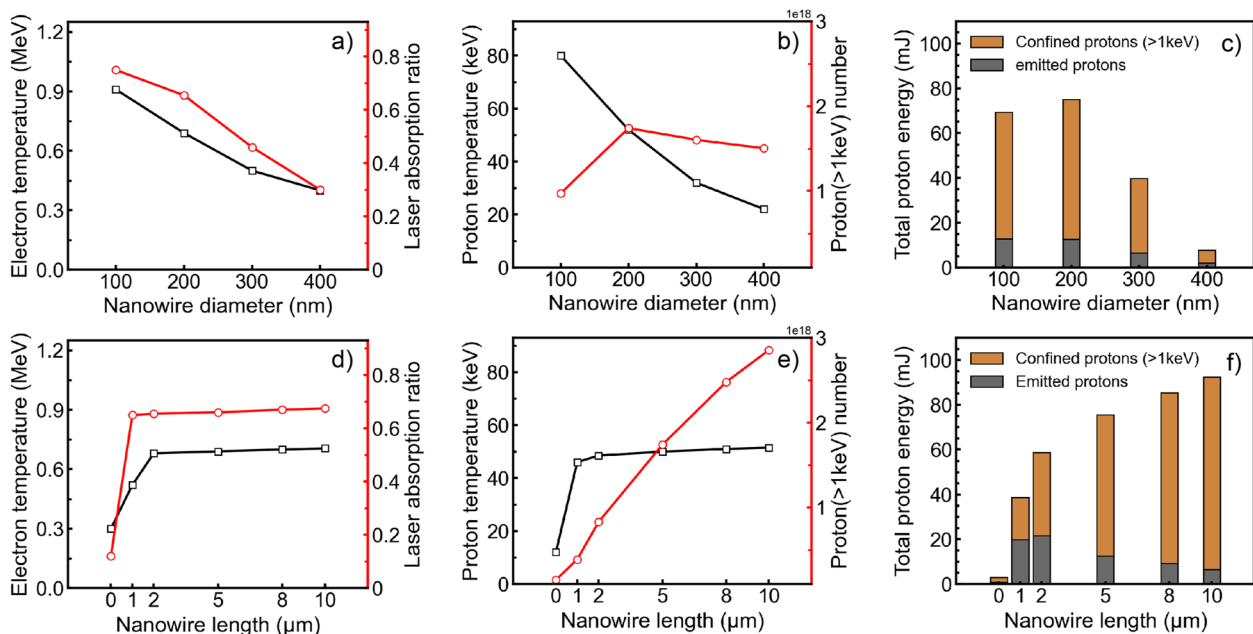
FIG. 6. Simulation results as functions of NW diameter: (a) laser absorption ratio and confined electron temperature, (b) confined proton temperature and number of confined protons (>1 keV), and (c) energy proportions of emitted and confined protons. Panels (d)–(f) show the same results as functions NW length. Other NWA parameters were $S = 450$ nm, $L = 5$ μm in panels (a)–(c) and $D = 200$ nm, $S = 450$ nm in panels (d)–(f).

of 200 nm were found to perform the best, in which 8% of the laser energy can be converted to confined protons.

IV. EXPERIMENTAL CAMPAIGN

Guided by the simulation results, we performed an experimental campaign to study the high-energy-density states in NWA targets. Confined ions are challenging to detect in experiments; instead, we measured the emitted ions to verify our conclusions.

The experiments were conducted on the Compact Laser Plasma Accelerator (CLAPA) laser facility at Peking University, which has a central wavelength of 800 nm and a pulse duration of 30 fs (full width at half maximum, FWHM). Figure 7(a) depicts a schematic of the experimental setup. A linearly polarized laser pulse was normally incident on the NWA target. To prevent the pre-expansion of NWs, a plasma mirror system was employed to improve the laser contrast ratio, ensuring that the intensity of the pre-pulse was below 10^{11} W/cm^2 at 5 ps.[55] We checked whether the NWs could maintain their structure under the irradiation of the ps pedestal before the main pulse by employing the hydrodynamic simulation code MULTI2D.[56] The results indicated the scale length of the pre-plasma $L_{\text{pre}} = n_e/(dn_e/dx) \sim 22$ nm, which is insignificant compared to the gaps between NWs. The laser energy was measured to be 3.5 ± 0.5 J before the compressor using a laser-energy meter. Considering that the energy transmission efficiencies of the beamlines and plasma mirror system are 40% and 75%, respectively, the on-target laser energy was about 1 J. Ultimately, the laser beam was focused into a spot size of 4.0–4.4 μm (FWHM) to reach an on-target peak intensity of 4.8×10^{19} W/cm^2 ($a_0 \sim 5$) by using an f/3, 90°, gold-coated off-axis-parabolic mirror (OAP). This OAP had a 3 mm-diameter hole that enabled ions from the front side of the target to pass to the ion spectrometer.

The ion spectra were measured using a Thomson parabola spectrometer (TPS) in the direction normal to the front side of the target. The TPS was composed of a collimating aperture, magnets, electrodes, a microchannel plate, a phosphor screen, and an electron-multiplying CCD (EMCCD). In this device, after the 1 mm-wide collimating aperture (1.3×10^{-6} Sr), collimated ions with different energies and charge-to-mass ratios (CMRs) are deflected by the electromagnetic fields and hit different positions on the microchannel plate. The ion signal multiplied by the microchannel plate is then converted to an optical signal at the phosphor screen and captured by the EMCCD. Ions with different CMRs have different parabolic traces imaged in TPS raw data. The set electric and measured magnetic fields of the TPS employed in the experiments were 0.83 kV/cm and 0.255 T, respectively. The detection area was limited by the microchannel plate, which had a diameter of 77 mm. Considering the electric field, magnetic field, and detection area, the energy range of protons was about 1–20 MeV. Furthermore, the angular distribution of emitted protons was recorded by CR39 iontrack detectors placed at angles of 20°, 40°, 55°, and 80° to the target normal.

Polyethylene NWA targets with a variety of parameters were examined in the experimental campaign. These were prepared by the following procedure. First, a thick polyethylene sheet was attached to an anodized aluminum oxide (AAO) template[57] with hexagonally packed nanochannels. Heating and mechanically compressing this sheet then caused the polyethylene molecules to move into the template. After this, an NWA target was obtained by dissolving the AAO membrane in a 2M NaOH solution for 30 min. The diameters, spacings, and lengths of the NWs were determined by the AAO templates. The morphologies of the NWAs were characterized by scanning electron microscopy (SEM), and typical top and side views are shown in Figs. 7(b) and 7(c), respectively. The thickness of the polyethylene substrate supporting the NWs was about 450 μm. The average density of the NWAs lay in the range of 16%–45% of the intrinsic solid density. Planar polyethylene targets with a thickness of 450 μm were used for comparison. Table I summarizes the parameters of all of the targets.

A. Measurements of the emitted protons

The experimental results of emitted protons for NWA targets with different lengths and diameters are summarized in Figs. 8(a) and 8(b), in which the error bars reflect the shot-to-shot fluctuations and the data points are the arithmetic means. The maximum proton energies of the planar targets are depicted by zero-diameter and zero-length points in Figs. 8(a) and 8(b). The solid lines represent the 2D PIC simulation results, which fit the experimental results. The corresponding best experimental proton spectra are displayed in Figs. 8(c) and 8(d), respectively. Compared to the planar targets, a
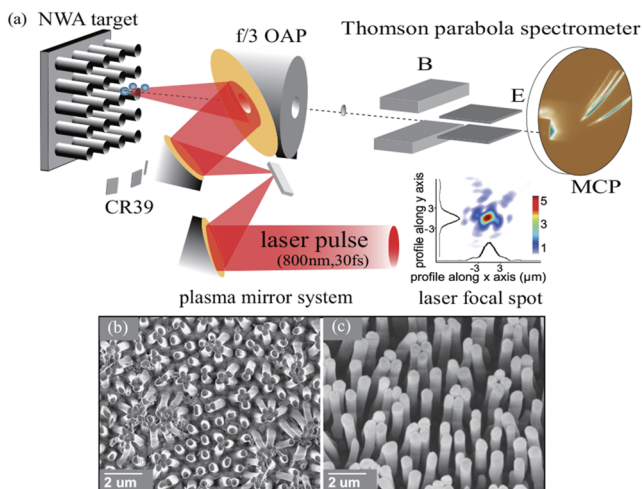
FIG. 7. (a) Schematic of the experimental setup. SEM images: (b) top and (c) side views of an NWA target.

TABLE I. Parameters of all NWA and planar targets.

Target	D (nm)	S (nm)	L (μm)	ρ_{av}/ρ_s	Thickness (μm)
NWA	200	450	1,2,4,5,10	0.16	
	300	450	5	0.35	450 ± 50
	500/600	800	5	0.31/0.45	
Planar	⋯	⋯	⋯	⋯	450 ± 50
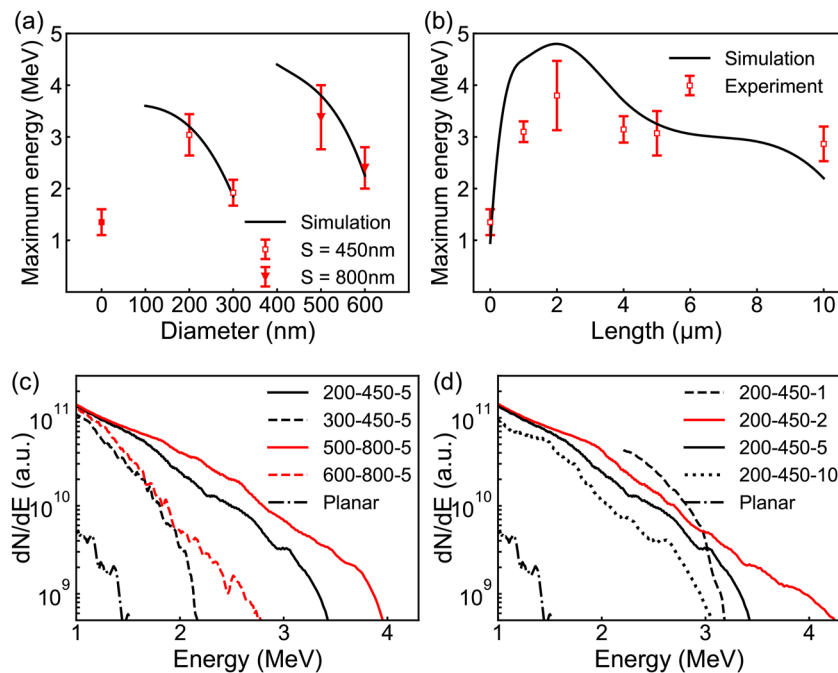
FIG. 8. Experimental and simulated maximum proton energy results for varying the (a) diameters and (b) lengths of the NWs in the array. The other parameters of the NWA are $S = 450$ nm/$S = 800$ nm, $L = 5$ μm in (a) and $D = 200$ nm, $S = 450$ nm in (b). Panels (c) and (d) depict the proton spectra in (a) and (b), respectively, in which an NWA target with $D = 200$ nm, $S = 450$ nm, and $L = 5$ μm is abbreviated as 200-450-5.

remarkable enhancement of maximum energy for NWA targets can be observed.

The dependence of the maximum proton energy on the NW diameter can be obtained from Figs. 8(a) and 8(c). For both $S = 450$ nm and $S = 800$ nm, the maximum proton energies decline with increasing NW diameter, which fits the simulation results well. For NWAs with fixed $D = 200$ nm and $S = 450$ nm, the maximum proton energies rise with increasing length until $L = 2$ μm, and they then decline. This trend reflects that the strongest E_{sx} is produced in the laser–plasma interactions for the 2 μm-length NWAs. When the NWs' length exceeds the optimal value, the laser pulse propagates more deeply into the NWA and transfers more of its energy to confined protons. It should be noted that our experimental results in relation to the emitted protons are consistent with those of another recent study.[58]

The angular distribution of emitted protons was measured by the CR39 detectors after 16 consecutive shots. 30 μm-thick aluminum foils were placed on the CR39 detectors, which can block most carbon ions below 32 MeV and protons below 1.6 MeV. Images of the etched CR39 detectors placed at 20°, 55°, and 80° to the target normal are displayed in Figs. 9(b)–9(d), respectively. They were etched for 12 h in 6M NaOH solution at 70 °C after shooting. The sizes of the three CR39 plates were identical, corresponding to a solid angle of 2×10^{-6} Sr. As one can see in Fig. 9(d), only a few protons were emitted at 80° with respect to the target normal. More proton tracks were observed with decreasing angle. The proton tracks (the small dots in the image) at 20° are very dense, even close to saturation. At 55°, a number of energetic proton tracks were observed, which implies that the divergence of the protons from the NWA was larger than for typical planar targets. In general, the CR39 results are inconsistent with our simulation results in Fig. 3(b). The most

energetic confined ions in lateral directions in Fig. 3(b) could not be detected as they had been stopped in the targets.

B. Deuterium and neutrons generated from deuterated polyethylene NWA

An NWA absorbs a majority of the laser energy and forms a near-solid-density HEDP, which creates excellent conditions for
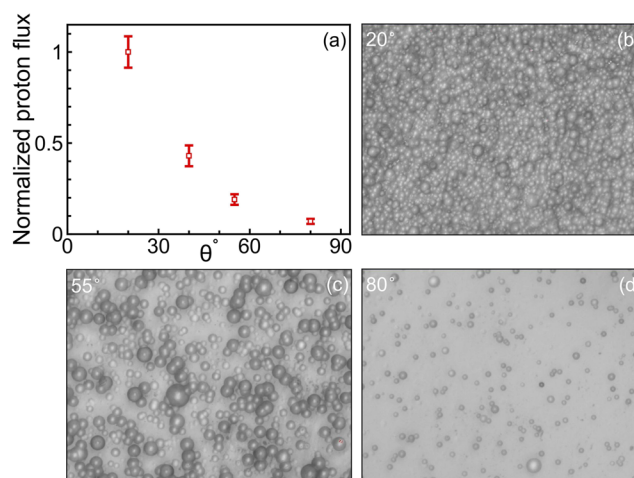
FIG. 9. (a) Angular distribution of protons; error bars represent the standard deviations of the statistics. Panels (b)–(d) show the raw data of CR39 surfaces with the same sizes at angles of 20°, 55°, and 80° with respect to the target normal, respectively.

charged-particle nuclear reactions. In the experimental campaign, we also employed deuterated polyethylene NWA targets to demonstrate the neutron generation from the ^{2}H(d,n)^{3}He fusion. They were prepared following the same procedure as the polyethylene NWAs.

We first tried to measure the deuterium ions (D$^+$) emitted from NWA targets using the TPS. The raw data, including all ions with different CMRs, are presented in Fig. 10(a). The traces with CMRs of 1, 1/2, ... can be identified. However, the traces of D$^+$ and C^{6+} are indistinguishable because they have the same CMR of 1/2. Therefore, we positioned a 20 μm-thick Al foil in front of the MCP to distinguish them. Due to different stopping powers, C^{6+} with energies <1.83 MeV/u will be blocked by the foil, while D$^+$ with energies >0.78 MeV/u can get through [see Fig. 10(c)]. This allows us to identify D$^+$ in the range 0.78–1.83 MeV/u on the MCP. Figure 10(b) displays the raw TPS data. The broadening of traces is due to the straggling of ions when they pass through the Al foil. The cut-off of the trace at the low-energy end corresponds to 0.8 MeV/u, which is very close to the theoretical value of 0.78 MeV/u. It is thus unambiguous that the remaining parabolic trace of CMR = 1/2 only results from the D$^+$.

The energy spectra of ions were obtained by analyzing the TPS traces, and these are shown in Figs. 10(d) and 10(e). The maximum proton energy of 3.5 MeV is similar to that without the Al foil, which indicates the good repeatability of the results. The maximum energy of the deuterium ions is 1.5 MeV/u, significantly lower than that of the protons. No deuterium-ion signal was detected for the planar deuterated polyethylene targets.

The observed emission of MeV-level deuterium is a signature of the strong laser–plasma coupling in the NWAs. Similar to the case of a polyethylene NWA, we performed 2D simulations to

study HEDP in a deuterated polyethylene NWA by employing the Smilei code.[59] The Smilei code includes a nuclear-reaction module, which can seamlessly simulate the ^{2}H(d,n)^{3}He fusion reaction using a Monte Carlo method. The nuclear-reaction module uses the relativistic kinematics calculations of the binary collision scheme in the COM frame.[60] New macroparticles (the reaction products) are created using a certain probability of a reaction occurring. The collision of deuterium with deuterium to create a neutron and helium was enabled in the simulation. Other simulation settings of Smilei, such as the box, laser, and target parameters, were the same as those in the EPOCH simulations.

Figure 11(a) shows the simulated energy density of deuterium ions in a deuterated NWA target with D = 200 nm, S = 450 nm, and L = 5 μm at t = 460 fs. The distribution of the energy density is very uniform, with a peak value of 0.22 GJ/cm^3. The peak temperature of the confined deuterium ions is 80 keV. The distribution of helium ions, which are the product of the fusion reactions, is depicted in Fig. 11(b). This indicates that nuclear reactions mainly occur in the focal-spot area where the temperature of the deuterium ions is highest. Figures 11(c) and 11(d) show the total helium yield (dashed lines) from NWAs with different lengths and diameters at t = 3 ps. Compared to a planar target, yields that are more than 20 times higher can be obtained from an optimal target. Increasing the NW length leads to increased yield; this, however, becomes less prominent when L exceeds 5 μm. The optimal diameter is D = 200 nm. The corresponding density is about 16% of the solid density.

The D–D nuclear reactions produce the same numbers of helium ions and neutrons. In a recent work, we reported the measurement of the neutrons from NWA targets with D = 200–500 nm, S = 450–800 nm, and L = 1–10 μm;[61] the average neutron yield per
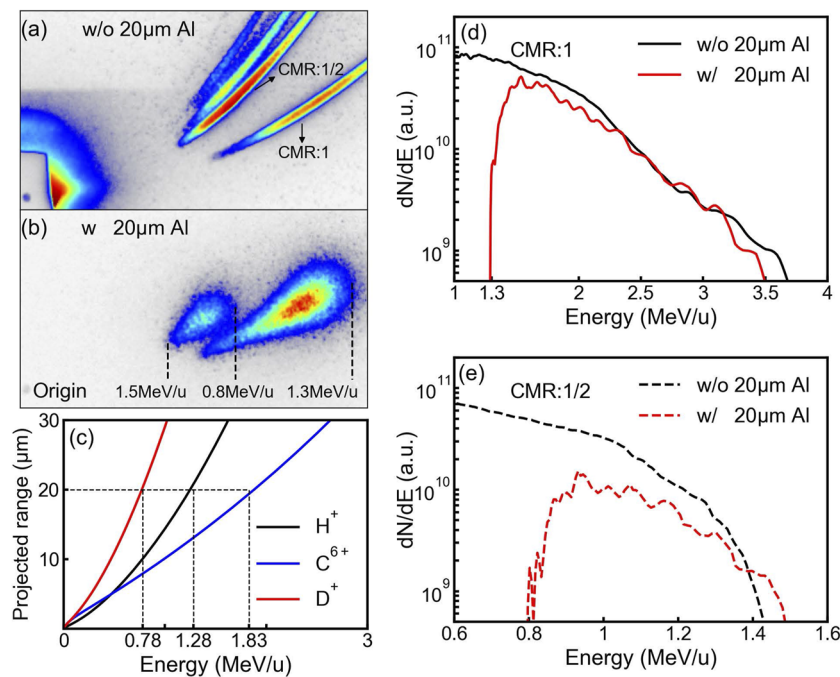
FIG. 10. Ion spectra: TPS raw data (a) without and (b) with 20 μm aluminum foil. (c) Projected range in aluminum foil for protons and deuterium and carbon ions. Energy spectra of ions with (d) CMR = 1 (proton) and (e) CMR = 1/2 (deuterium or carbon ion).
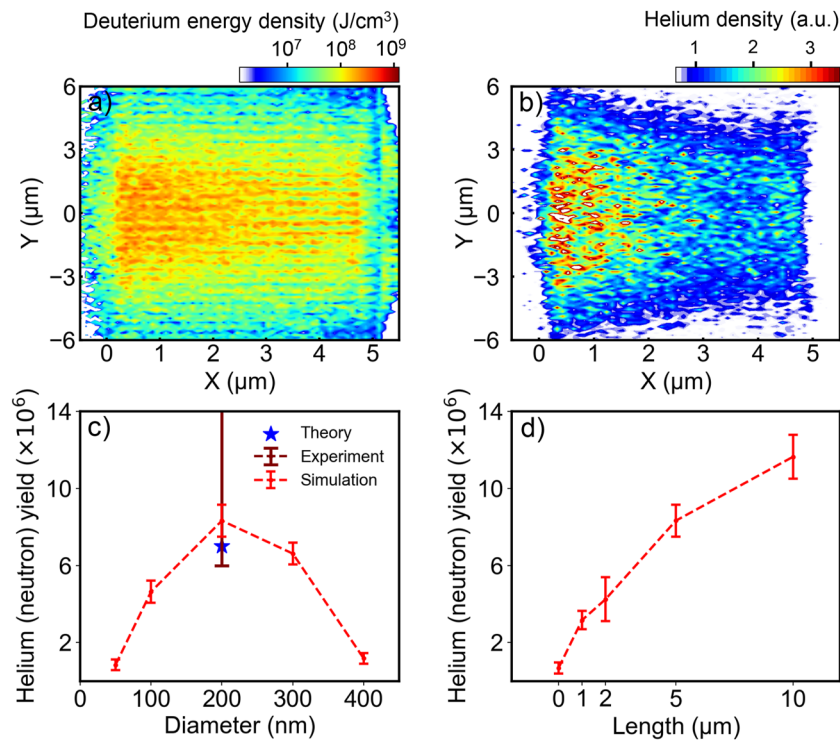
FIG. 11. (a) Deuterium energy density at a simulation time of $t = 460$ fs. (b) Spatial distribution of the density of helium ions at $t = 460$ fs. Simulated helium (neutron) yield for different NW (c) lengths and (d) diameters at a simulation time of $t = 3$ ps. The error bars represent the statistical fluctuations. The theoretical value of neutron yield from an NWA target with $D = 200$ nm, $S = 450$ nm, and $L = 5$ μm and the average neutron yield in the experiments from different NWA parameters are also shown in panel (c).

shot was $(24 \pm 18) \times 10^6$/J. One can see that the simulation results of the present work agree well with our previous observations.

We can also theoretically estimate the neutron yield. The volumetric reaction rate is given by $R = n_D^2 \sigma \vartheta_r / (1 + \delta)$, where: n_D is the average deuterium ion density of $16\% \times 8 \times 10^{22}$ cm^{-3} for an NWA target with $D = 200$ nm, $S = 450$ nm, and $L = 5$ μm; ϑ_r is the deuterium–deuterium relative velocity, which we take as $2\vartheta_D \sim c/54$ based on the deuterium ion temperature of 80 keV; σ is the corresponding fusion cross section of 0.085 b[62] for a deuterium ion energy of 160 keV in the center-of-mass frame; and δ is the Kronecker symbol of 1. Therefore, the reaction numbers can be roughly estimated as $N = V n_D^2 \sigma \vartheta_r \tau / 2$, multiplied by the reaction volume V and the reaction time τ. The value of V is about 6×10^{-10} cm^{-3} considering a cylindrical reaction area of 6 μm radius and 5 μm length. The value of τ can be roughly estimated as $V^{1/3}/\vartheta_D \sim 2.8$ ps. According to the above analysis, the number of neutrons $N \sim 7 \times 10^6$ in 4π, which is in agreement with the experimental and simulation results.

V. CONCLUSION

In conclusion, we numerically and experimentally studied the HEDP formed in femtosecond-laser-irradiated NWA targets. It was found that the unique structure of the NWs leads to the generation of rich, energetic ions, which are eventually confined in the plasma and contribute most to the high-energy-density state. The emitted ions can be used as valuable diagnostics of the interaction. Our systematic study on the dependence of the ion energy density on the parameters of the NWA targets illustrates the optimal parameters for the generation of HEDP in NWAs and gives a valuable guide for future works employing NWA targets. The achieved large-volume homogeneous GJ/cm^3-level energy density of ions driven by merely J-level lasers can provide a valuable testbed for high-energy-density and nuclear physics.

AUTHOR DECLARATIONS

Conflict of Interest

The authors have no conflicts to disclose.

Author Contributions

Defeng Kong: Conceptualization (equal); Data curation (equal); Formal analysis (equal); Investigation (equal); Methodology (equal); Validation (equal); Visualization (equal); Writing – original draft (equal). **Guoqiang Zhang**: Conceptualization (equal); Methodology (equal); Validation (equal); Writing – review & editing (equal).

Yinren Shou: Methodology (equal); Validation (equal). **Shirui Xu**: Methodology (equal); Validation (equal). **Zhusong Mei**: Methodology (equal); Validation (equal). **Zhengxuan Cao**: Methodology (equal); Validation (equal). **Zhuo Pan**: Methodology (equal); Validation (equal). **Pengjie Wang**: Methodology (equal); Validation (equal). **Guijun Qi**: Methodology (equal); Validation (equal). **Yao Lou**: Methodology (equal); Validation (equal). **Zhiguo Ma**: Methodology (equal); Validation (equal). **Haoyang Lan**: Methodology (equal); Validation (equal). **Wenzhao Wang**: Methodology (equal); Validation (equal). **Yunhui Li**: Validation (equal). **Peter Rubovic**: Methodology (equal); Validation (equal); Writing – review & editing (equal). **Martin Veselsky**: Methodology (equal); Validation (equal); Writing – review & editing (equal). **Aldo Bonasera**: Funding acquisition (equal); Writing – review & editing (equal). **Jiarui Zhao**: Methodology (equal); Validation (equal). **Yixing Geng**: Methodology (equal); Validation (equal). **Yanying Zhao**: Methodology (equal); Validation (equal). **Changbo Fu**: Methodology (equal); Validation (equal). **Wen Luo**: Methodology (equal); Validation (equal); Writing – review & editing (equal). **Yugang Ma**: Methodology (equal); Validation (equal). **Xueqing Yan**: Writing – review & editing (equal). **Wenjun Ma**: Conceptualization (equal); Funding acquisition (equal); Methodology (equal); Validation (equal); Writing – review & editing (equal).

DATA AVAILABILITY

Data available on request from the authors.

REFERENCES

[1] V. E. Fortov, "High Energy Densities in Planets and Stars," *Extreme States of Matter: High Energy Density Physics* (Springer International Publishing, Cham, 2016), pp. 505–590.

[2] D. Kasen, B. Metzger, J. Barnes, E. Quataert, and E. Ramirez-Ruiz, "Origin of the heavy elements in binary neutron-star mergers from a gravitational-wave event," Nature **551**(7678), 80–84 (2017).

[3] J. P. Freidberg, *Plasma Physics and Fusion Energy* (Cambridge University Press, 2008).

[4] M. Roth, T. E. Cowan, M. H. Key, S. P. Hatchett, C. Brown, W. Fountain *et al.*, "Fast ignition by intense laser-accelerated proton beams," Phys. Rev. Lett. **86**(3), 436–439 (2001).

[5] R. Betti and O. A. Hurricane, "Inertial-confinement fusion with lasers," Nat. Phys. **12**(5), 435–448 (2016).

[6] R. S. Craxton, K. S. Anderson, T. R. Boehly, V. N. Goncharov, D. R. Harding, J. P. Knauer *et al.*, "Direct-drive inertial confinement fusion: A review," Phys. Plasmas **22**(11), 110501 (2015).

[7] O. A. Hurricane, D. A. Callahan, D. T. Casey, P. M. Celliers, C. Cerjan, E. L. Dewald *et al.*, "Fuel gain exceeding unity in an inertially confined fusion implosion," Nature **506**(7488), 343–348 (2014).

[8] C. Labaune, C. Baccou, S. Depierreux, C. Goyon, G. Loisel, V. Yahia, and J. Rafelski, "Fusion reactions initiated by laser-accelerated particle beams in a laser-produced plasma," Nat. Commun. **4**, 2506 (2013).

[9] D. T. Casey, D. B. Sayre, C. R. Brune, V. A. Smalyuk, C. R. Weber, R. E. Tipton *et al.*, "Thermonuclear reactions probed at stellar-core conditions with laser-based inertial-confinement fusion," Nat. Phys. **13**(12), 1227–1231 (2017).

[10] I. Hofmann, "Review of accelerator driven heavy ion nuclear fusion," Matter Radiat. Extremes **3**(1), 1–11 (2018).

[11] L. Fedeli, A. Formenti, A. Pazzaglia, F. M. Arioli, A. Tentori, and M. Passoni, "Enhanced laser-driven hadron sources with nanostructured double-layer targets," New J. Phys. **22**(3), 033045 (2020).

[12] W. Bang, M. Barbui, A. Bonasera, G. Dyer, H. J. Quevedo, K. Hagel *et al.*, "Temperature measurements of fusion plasmas produced by Petawatt-Laser-Irradiated $D_2{}^3He$ or $CD_4{}^3He$ clustering gases," Phys. Rev. Lett. **111**(5), 055002 (2013).

[13] M. Barbui, W. Bang, A. Bonasera, K. Hagel, K. Schmidt, J. B. Natowitz *et al.*, "Measurement of the plasma astrophysical S factor for the $^3He(d, p)^4He$ reaction in exploding molecular clusters," Phys. Rev. Lett. **111**(8), 082502 (2013).

[14] G. Zhang, H. J. Quevedo, A. Bonasera, M. Donovan, G. Dyer, E. Gaul *et al.*, "Range of plasma ions in cold cluster gases near the critical point," Phys. Lett. A **381**(19), 1682–1686 (2017).

[15] G. Zhang, M. Huang, A. Bonasera, Y. G. Ma, B. F. Shen, H. W. Wang *et al.*, "Nuclear probes of an out-of-equilibrium plasma at the highest compression," Phys. Lett. A **383**(19), 2285–2289 (2019).

[16] S. Fujioka, H. Takabe, N. Yamamoto, D. Salzmann, F. Wang, H. Nishimura *et al.*, "X-ray astronomy in the laboratory with a miniature compact object produced by laser-driven implosion," Nat. Phys. **5**(11), 821–825 (2009).

[17] A. J. Kemp, S. C. Wilks, E. P. Hartouni, and G. Grim, "Generating keV ion distributions for nuclear reactions at near solid-density using intense short-pulse lasers," Nat. Commun. **10**(1), 4156 (2019).

[18] M. K. Matzen, "Z pinches as intense x-ray sources for high-energy density physics applications," Phys. Plasmas **4**(5), 1519–1527 (1997).

[19] R. P. Drake, "Introduction to high-energy-density physics," *High-Energy-Density Physics: Foundation of Inertial Fusion and Experimental Astrophysics* (Springer International Publishing, Cham, 2018), pp. 1–20.

[20] M. Huang, H. J. Quevedo, G. Zhang, and A. Bonasera, "Nuclear astrophysics with lasers," Nucl. Phys. News **29**(3), 9–13 (2019).

[21] P. Wang, Z. Gong, S. G. Lee, Y. Shou, Y. Geng, C. Jeon *et al.*, "Super-heavy ions acceleration driven by ultrashort laser pulses at ultrahigh intensity," Phys. Rev. X **11**(2), 021049 (2021).

[22] O. N. Rosmej, Z. Samsonova, S. Höfer, D. Kartashov, C. Arda, D. Khaghani *et al.*, "Generation of keV hot near-solid density plasma states at high contrast laser-matter interaction," Phys. Plasmas **25**(8), 083103 (2018).

[23] J. H. Bin, W. J. Ma, H. Y. Wang, M. J. Streeter, C. Kreuzer, D. Kiefer *et al.*, "Ion acceleration using relativistic pulse shaping in near-critical-density plasmas," Phys. Rev. Lett. **115**(6), 064801 (2015).

[24] I. Prencipe, A. Sgattoni, D. Dellasega, L. Fedeli, L. Cialfi, I. W. Choi *et al.*, "Development of foam-based layered targets for laser-driven ion beam production," Plasma Phys. Controlled Fusion **58**(3), 034019 (2016).

[25] J. H. Bin, M. Yeung, Z. Gong, H. Y. Wang, C. Kreuzer, M. L. Zhou *et al.*, "Enhanced laser-driven ion acceleration by superponderomotive electrons generated from near-critical-density plasma," Phys. Rev. Lett. **120**(7), 074801 (2018).

[26] W. J. Ma, I. J. Kim, J. Q. Yu, I.W. Choi, P. K. Singh, H. W. Lee *et al.*, "Laser acceleration of highly energetic carbon ions using a double-layer target composed of slightly underdense plasma and ultrathin foil," Phys. Rev. Lett. **122**(1), 014803 (2019).

[27] R. Hollinger, C. Bargsten, V. N. Shlyaptsev, V. Kaymak, A. Pukhov, M. G. Capeluto *et al.*, "Efficient picosecond x-ray pulse generation from plasmas in the radiation dominated regime," Optica **4**(11), 1344 (2017).

[28] C. Bargsten, R. Hollinger, M. G. Capeluto, V. Kaymak, A. Pukhov, S. Wang *et al.*, "Energy penetration into arrays of aligned nanowires irradiated with relativistic intensities: Scaling to terabar pressures," Sci. Adv. **3**(1), e1601558 (2017).

[29] L. L. Ji, J. Snyder, A. Pukhov, R. R. Freeman, and K. U. Akli, "Towards manipulating relativistic laser pulses with micro-tube plasma lenses," Sci. Rep. **6**, 23256 (2016).

[30] G. Cristoforetti, P. Londrillo, P. K. Singh, F. Baffigi, G. D'Arrigo, A. D. Lad *et al.*, "Transition from Coherent to Stochastic electron heating in ultrashort relativistic laser interaction with structured targets," Sci. Rep. **7**(1), 1479 (2017).

[31] L.-q. Zhang, S.-d. Wu, H.-r. Huang, H.-y. Lan, W.-y. Liu, Y.-c. Wu *et al.*, "Brilliant attosecond γ-ray emission and high-yield positron production from intense laser-irradiated nano-micro array," Phys. Plasmas **28**(2), 023110 (2021).

[32] O. V. Gotchev, P. Y. Chang, J. P. Knauer, D. D. Meyerhofer, O. Polomarov, J. Frenje *et al.*, "Laser-driven magnetic-flux compression in high-energy-density plasmas," Phys. Rev. Lett. **103**(21), 215004 (2009).

[33]K. Jiang, A. Pukhov, and C. T. Zhou, "TJ cm^{-3} high energy density plasma formation from intense laser-irradiated foam targets composed of disordered carbon nanowires," Plasma Phys. Controlled Fusion **63**(1), 015014 (2020).

[34]X. Z. Wu, Z. Gong, Y. R. Shou, Y. H. Tang, J. Q. Yu, G. Mourou et al., "Efficiency enhancement of ion acceleration from thin target irradiated by multi-PW few-cycle laser pulses," Phys. Plasmas **28**(2), 023102 (2021).

[35]E. Eftekhari-Zadeh, M. S. Blümcke, Z. Samsonova, R. Loetzsch, I. Uschmann, M. Zapf et al., "Laser energy absorption and x-ray generation in nanowire arrays irradiated by relativistically intense ultra-high contrast femtosecond laser pulses," Phys. Plasmas **29**(1), 013301 (2022).

[36]R. Xie, L. H. Cao, Y. Chao, Y. Jiang, Z. J. Liu, C. Y. Zheng et al., "Improvement of laser absorption and control of particle acceleration by subwavelength nanowire target," Phys. Plasmas **27**(12), 123108 (2020).

[37]S. Jiang, A. G. Krygier, D. W. Schumacher, K. U. Akli, and R. R. Freeman, "Effects of front-surface target structures on properties of relativistic laser-plasma electrons," Phys. Rev. E **89**(1), 013106 (2014).

[38]V. Kaymak, A. Pukhov, V. N. Shlyaptsev, and J. J. Rocca, "Nanoscale ultradense Z-pinch formation from laser-irradiated nanowire arrays," Phys. Rev. Lett. **117**(3), 035004 (2016).

[39]L. Cao, Y. Gu et al., "Enhanced absorption of intense short-pulse laser light by subwavelength nanolayered target," Phys. Plasmas **17**(4), 043103 (2010)..

[40]R. A. Snavely, M. H. Key, S. P. Hatchett, T. E. Cowan, M. Roth, T. W. Phillips et al., "Intense high-energy proton beams from petawatt-laser irradiation of solids," Phys. Rev. Lett. **85**(14), 2945–2948 (2000).

[41]F. Wagner, O. Deppert, C. Brabetz, P. Fiala, A. Kleinschmidt, P. Poth et al., "Maximum proton energy above 85 MeV from the relativistic interaction of laser pulses with micrometer thick CH$_2$ targets," Phys. Rev. Lett. **116**(20), 205002 (2016).

[42]B. Li, Z. Zhang, J. Wang, B. Zhang, Z. Zhao, L. Shan et al., "Transport of fast electrons in a nanowire array with collisional effects included," Phys. Plasmas **22**(12), 123118 (2015).

[43]D. Khaghani, M. Lobet, B. Borm, L. Burr, F. Gärtner, L. Gremillet et al., "Enhancing laser-driven proton acceleration by using micro-pillar arrays at high drive energy," Sci. Rep. **7**(1), 11366 (2017).

[44]M. Dozières, G. M. Petrov, P. Forestier-Colleoni, P. Campbell, K. Krushelnick, A. Maksimchuk et al., "Optimization of laser-nanowire target interaction to increase the proton acceleration efficiency," Plasma Phys. Controlled Fusion **61**(6), 065016 (2019).

[45]M. A. Purvis, V. N. Shlyaptsev, R. Hollinger, C. Bargsten, A. Pukhov, A. Prieto et al., "Relativistic plasma nanophotonics for ultrahigh energy density physics," Nat. Photonics **7**(10), 796–800 (2013).

[46]D. Rolles, "Highly efficient nanoscale X-ray sources," Nat. Photonics **12**(2), 59–60 (2018).

[47]W.-M. Wang, Z.-M. Sheng, P. Gibbon, L.-M. Chen, Y.-T. Li, and J. Zhang, "Collimated ultrabright gamma rays from electron wiggling along a petawatt laser-irradiated wire in the QED regime," Proc. Natl. Acad. Sci. U. S. A. **115**(40), 9911–9916 (2018).

[48]Y. Shou, D. Kong, P. Wang, Z. Mei, Z. Cao, Z. Pan et al., "High-efficiency water-window x-ray generation from nanowire array targets irradiated with femtosecond laser pulses," Opt. Express **29**(4), 5427–5436 (2021).

[49]A. Curtis, C. Calvi, J. Tinsley, R. Hollinger, V. Kaymak, A. Pukhov et al., "Micro-scale fusion in dense relativistic nanowire array plasmas," Nat. Commun. **9**(1), 1077 (2018).

[50]A. Curtis, R. Hollinger, C. Calvi, S. Wang, S. Huanyu, Y. Wang et al., "Ion acceleration and D-D fusion neutron generation in relativistically transparent deuterated nanowire arrays," Phys. Rev. Res. **3**(4), 043181 (2021).

[51]S. H. Glenzer, D. A. Callahan, A. J. MacKinnon, J. L. Kline, G. Grim, E. T. Alger et al., "Cryogenic thermonuclear fuel implosions on the national ignition facility," Phys. Plasmas **19**(5), 056318 (2012).

[52]R. Hollinger, S. Wang, Y. Wang, A. Moreau, M. G. Capeluto, H. Song et al., "Extreme ionization of heavy atoms in solid-density plasmas by relativistic second-harmonic laser pulses," Nat. Photonics **14**(10), 607–611 (2020).

[53]T. D. Arber, K. Bennett, C. S. Brady, A. Lawrence-Douglas, M. G. Ramsay, N. J. Sircombe et al., "Contemporary particle-in-cell approach to laser-plasma modelling," Plasma Phys. Controlled Fusion **57**(11), 113001 (2015).

[54]Z. Gong, A. P. L. Robinson, X. Q. Yan, and A. V. Arefiev, "Highly collimated electron acceleration by longitudinal laser fields in a hollow-core target," Plasma Phys. Controlled Fusion **61**(3), 035012 (2019).

[55]Y.-X. Geng, L. Qing, Y.-R. Shou, J.-G. Zhu, X.-H. Xu, M.-J. Wu et al., "Generating proton beams exceeding 10 MeV using high contrast 60 TW laser," Chin. Phys. Lett. **35**(9), 092901 (2018).

[56]R. Ramis, R. Schmalz, and J. Meyer-Ter-Vehn, "MULTI— a computer code for one-dimensional multigroup radiation hydrodynamics," Comput. Phys. Commun. **49**(3), 475–505 (1988).

[57]X. Wang and G.-R. Han, "Fabrication and characterization of anodic aluminum oxide template," Microelectron. Eng. **66**(1-4), 166–170 (2003).

[58]S. Vallières, M. Salvadori, A. Permogorov, G. Cantono, K. Svendsen, Z. Chen et al., "Enhanced laser-driven proton acceleration using nanowire targets," Sci. Rep. **11**(1), 2226 (2021).

[59]J. Derouillat, A. Beck, F. Pérez, T. Vinci, M. Chiaramello, A. Grassi et al., "SMILEI: A collaborative, open-source, multi-purpose particle-in-cell code for plasma simulation," Comput. Phys. Commun. **222**, 351–373 (2018).

[60]D. P. Higginson, A. Link, and A. Schmidt, "A pairwise nuclear fusion algorithm for weighted particle-in-cell plasma simulations," J. Comput. Phys. **388**, 439–453 (2019).

[61]P. Rubovič, A. Bonasera, P. Burian, Z. Cao, C. Fu, D. Kong et al., "Measurements of D–D fusion neutrons generated in nanowire array laser plasma using Timepix3 detector," Nucl. Instrum. Methods Phys. Res., Sect. A **985**, 164680 (2021).

[62]S. Glasstone and R. H. Lovberg, *Controlled Thermonuclear Reactions: An Introduction to Theory and Experiment* (van Nostrand Princeton, 1960).